Demonstration Of Rabi-Flops With Ytterbium 171 Trapped-Ion Qubits

Naleli Matjelo[1], Nancy Payne[1], Charles Rigby[1], Ncamiso Khanyile[1]

[1]Stellenbosch University, Physics Department, Laser Research Institute, Stellenbosch, South Africa.

DOI: 10.29322/IJSRP.11.07.2021.p11519
http://dx.doi.org/10.29322/IJSRP.11.07.2021.p11519

Abstract: *This paper presents a proof-of-concept for manipulation of Ytterbium 171 trapped-ion qubits through the Rabi-flops experiment. This serves as a partial report on an ongoing project aimed at developing a fully operational ion trapping and quantum feedback control laboratory at Stellenbosch University. Despite the bad vacuum conditions during the Rabi-flops experiment, we were able to manipulate the trapped Ytterbium 171 ion qubits with microwave pulses to give out a clear indication of Rabi oscillations. A high rate of ion loss led to the Rabi oscillations profile showing a decay feature within it. This decay feature was modeled and characterized, hence showing that we were losing ions at the rate defined by a time constant of* $\tau = 4500^{-1}$ *seconds.*

Keywords: Ytterbium, Trapped Ion, Qubit, Rabi-flops, Photoionization, Doppler Cooling, State Preparation, Evolution, Detection.

I. INTRODUCTION

Ions with a single electron in the valence shell have a relatively simple and manageable electronic level structure which simplifies the laser-cooling of such alkali-like ions. Among the good candidates there Be^+, Mg^+, Ca^+, Sr^+, and Ba^+ from group $A\ II$ earth alkalies, Zn^+, Cd^+ and Hg^+ from group $B\ II$ transition metals and Yb^+ from the Lanthanide series. More details of the required electronic configuration can be found in [1]. The method whereby any of these can be used as a qubit depends on the detailed electronic structure. One type of trapped ion qubit is the optical qubit [2] which makes use of the electronic ground state and a metastable excited electronic state of a trapped ion as the qubit's ground and excited states respectively. The energy difference between these two electronic states matches the energy of the photon from a driving optical laser. Fig. 1 below shows a typical structure of an optical qubit.

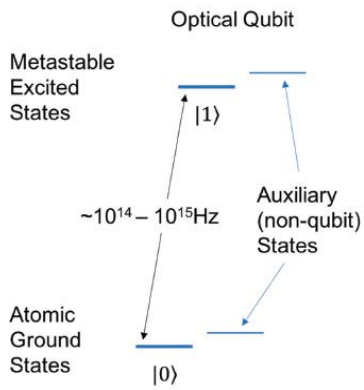

Fig. 1 Optical qubit energy levels.

Optical qubits, such as one realized from Calcium ion, have coherence times in the range of 1 to 30 seconds and the efficiency in their preparation and detection exceeds 99.9% [2]. Ions with low-lying D levels have the possibility of encoding a qubit in the $S \leftrightarrow D$ optical transition. However, the D level natural spectral width (a few Hz) requires laser fractional frequency stability of the order of 10^{-14} and this difficulty renders the optical ion qubit choice less common [1]. Ions with zero nuclear spin have only two Zeeman states in the $S_{1/2}$ level, which corresponds to the valence electron spin pointing parallel and anti-parallel to the external magnetic field direction [1], [3], [4]. Encoding a qubit in a pair of $S_{1/2}$ levels have the advantage of a practically infinite spontaneous decay time. Fig. 2 below shows a typical Zeeman qubit level structure.

This publication is licensed under Creative Commons Attribution CC BY.

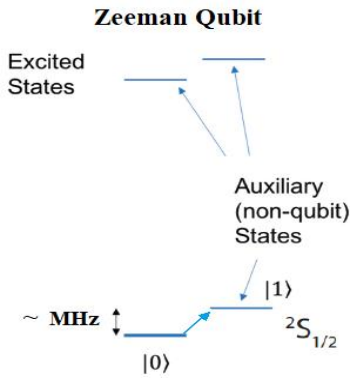

Fig. 2 Zeeman qubit energy levels.

An advantage of choosing this qubit is that since the qubit levels are the only levels in the $S_{1/2}$ manifold, optical pumping out of the qubit manifold does not occur however, the disadvantage of the Zeeman qubit is that since the energy difference between the two-qubit states depends linearly on the magnetic field, magnetic field noise will cause dephasing [4]. Furthermore, at low magnetic fields, the frequency separation between the two-qubit states is smaller than the P level natural spectral width, and therefore, state selective fluorescence cannot be directly applied for qubit state detection [1]. In odd isotopes or even isotopes with non-zero nuclear spin, the $S_{1/2}$ is split into different mF states within the different F-hyperfine manifolds with the energy separations in the gigahertz for common ions like ytterbium 171. A qubit can be encoded in any pair of hyperfine states [1]. Fig. 3 below shows an example of hyperfine qubit levels for ytterbium 171.

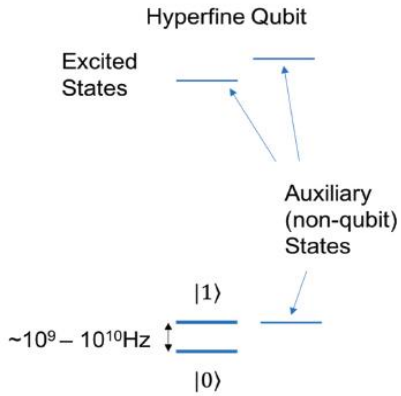

Fig. 3 Hyperfine qubit energy levels.

An advantage of the hyperfine qubit choice is that pairs of levels can be found such that their energy separation does not depend, to first order, on the magnetic field [1]. This paper covers the concepts and techniques involved in trapping, cooling, and manipulating Ytterbium ions. Although ytterbium has many isotopes we focus mainly on $^{171}Yb^+$. The rest of this paper is organized as follows. Section II gives some theoretical background on the interaction between a trapped ion and laser radiation. Section III gives a brief account of the isotope-selective ionization process of ytterbium atoms. Trapping parameters and Doppler cooling are briefly discussed in Section III. Section IV demonstrates $^{171}Yb^+$ qubit by showing Rabi flops with a small ion cloud. Section V concludes this paper with some remarks on major findings and some anticipated future work.

II. MAGNETIC DIPOLE TRANSITIONS

Electromagnetic radiation can be used to operate on the qubit state, in which resonant optical fields drive optical qubit states while the hyperfine qubit states are driven by resonant microwave fields or by a pair of lasers detuned from each other by the qubit microwave frequency (Raman transitions) [2]. The following account on the magnetic dipole transitions is adopted from [5] and similar accounts using electric dipole moment appear in other references including [6], [7]. Since our system uses Ytterbium hyperfine qubits, we describe the physics of magnetic dipole allowed transitions. The perturbative Hamiltonian due to the radiation is given by,

$$\hat{H}_I = -\hat{\mu}_z B_0 cos(\omega t + \delta_0) \quad (1)$$

with $\hat{\mu}_z$ as the z-component of the atom's magnetic moment, ω is the applied radiation angular frequency, B_0 is the amplitude of the radiation, and δ_0 is the phase. Considering small perturbation to the system, and expanding the system's wave function in terms of unperturbed Hamiltonian eigenstates we get,

$$|\psi(t)\rangle = \sum_m c_m(t) e^{-\frac{iE_m t}{\hbar}} |m\rangle \quad (2)$$

Substituting into the time-dependent Schrodinger equation we get,

$$i\hbar \dot{c}_n e^{-\frac{iE_n t}{\hbar}} = \sum_m c_m e^{-\frac{iE_m t}{\hbar}} \langle n|\hat{H}|m\rangle \quad (3)$$

with $\hat{H} = \hat{H}_0 + \hat{H}_I$, with $\hat{H}|m\rangle = E_m |m\rangle$. In the magnetic dipole approximation, the wavelength of the magnetic radiation is much larger than the spatial extent of the atomic wave function and we can write $\langle n|\hat{H}|m\rangle = -B_0 \cos(\omega t + \delta_0)\langle n|\hat{\mu}_z|m\rangle$. The quantity $\langle n|\hat{\mu}_z|m\rangle$ is non-zero only for $n \neq m$ due to odd parity. We focus on a transition of the two-level system $|0\rangle$ and $|1\rangle$ such as one shown in Fig. 4 below whereby equation (3) above results in the following set of coupled differential equations,

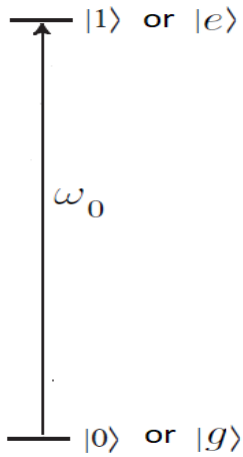

Fig. 4 Schematic level structure of a two-level system.

$$i\hbar \dot{c}_0 = -c_1 d_{10} B_0 e^{-i\omega_{10} t} \cos(\omega t + \delta_0) \quad (4)$$

$$i\hbar \dot{c}_1 = -c_0 d_{10}^* B_0 e^{+i\omega_{10} t} \cos(\omega t + \delta_0) \quad (5)$$

with $\omega_{10} = \frac{E_1 - E_0}{\hbar}$ and d_{10} as the magnetic dipole matrix element. In the rotating wave approximation, we get the following,

$$\dot{c}_0 = -\frac{i\Omega}{2} c_1 e^{+i(\Delta t + \delta_0)} \quad (6)$$

$$\dot{c}_1 = -\frac{i\Omega}{2} c_0 e^{-i(\Delta t + \delta_0)} \quad (7)$$

with $\Omega = d_{10}.B_0/\hbar$ as the Rabi frequency, $\Delta = \omega - \omega_{10}$ is the detuning and ω is the laser frequency. Further algebra yields the following second differential equation,

$$\ddot{c}_1 + i\Delta \dot{c}_1 + \left|\frac{\Omega}{2}\right|^2 c_1 = 0 \quad (8)$$

whose solution is given by,

$$c_1(t) = e^{-\frac{i\Delta t}{2}} \left(a e^{-\frac{i\Omega_R t}{2}} + b e^{-\frac{i\Omega_R t}{2}} \right) \quad (9)$$

with $\Omega_R = \sqrt{\Omega^2 + \Delta^2}$ as the generalized Rabi frequency, a and b can be obtained from initial conditions. Given an ion that starts in the ground state $|0\rangle$ at time $t = 0$, with initial conditions $c_0(0) = 1$ and $c_1(0) = 0$, hence $b = -a$, we get,

$$c_1(t) = -2ai e^{-\frac{i\Delta t}{2}} \sin\left(\frac{\Omega_R t}{2}\right) \quad (10)$$

From the initial conditions $c_0(0) = 1$ and $c_1(0) = 0$, we arrive at the solution,

$$c_1(t) = \frac{i\Omega^*}{\Omega_R} e^{-i\left(\frac{\Delta t}{2} + \delta_0\right)} \sin\left(\frac{\Omega_R t}{2}\right) \quad (11)$$

$$c_0(t) = e^{\frac{i\Delta t}{2}} \left[\cos\left(\frac{\Omega_R t}{2}\right) - \frac{i\Delta}{\Omega_R} \sin\left(\frac{\Omega_R t}{2}\right) \right] \quad (12)$$

This publication is licensed under Creative Commons Attribution CC BY.

On the flip-side, the initial conditions $c_1(0) = 1$ and $c_0(0) = 0$ lead to the solution as,

$$c_1(t) = \frac{i\Omega}{\Omega_R} e^{i\left(\frac{\Delta t}{2}+\delta_0\right)} sin\left(\frac{\Omega_R t}{2}\right) \tag{13}$$

$$c_0(t) = e^{-\frac{i\Delta t}{2}}\left[cos\left(\frac{\Omega_R t}{2}\right) + \frac{i\Delta}{\Omega_R} sin\left(\frac{\Omega_R t}{2}\right)\right] \tag{14}$$

These two solution sets can be used to describe arbitrary microwave operations on the qubit. Any arbitrary initial state is simply a superposition of $|0\rangle$ and $|1\rangle$; e.g. $|\psi\rangle = \alpha|0\rangle + \beta|1\rangle$ with $\alpha^2 + \beta^2 = 1$. The arbitrary operation $R_{\mu w}$ acting on j i is then $R_{\mu w}|\psi\rangle = \alpha R_{\mu w}|0\rangle + \beta R_{\mu w}|1\rangle$. Thus, if we know the action of $R_{\mu w}$ on $|0\rangle$ and $|1\rangle$, we know the action of $R_{\mu w}$ on any state. Given that the qubit states are described as $|0\rangle = [1,0]^T$ and $|1\rangle = [0,1]^T$, it can be shown that the full microwave operation matrix acting on an arbitrary qubit state has the following form,

$$R_{\mu w} = \begin{bmatrix} e^{\frac{i\Delta t}{2}}\left[cos\left(\frac{\Omega_R t}{2}\right) - \frac{i\Delta}{\Omega_R} sin\left(\frac{\Omega_R t}{2}\right)\right] & \frac{i\Omega}{\Omega_R} e^{i\left(\frac{\Delta t}{2}+\delta_0\right)} sin\left(\frac{\Omega_R t}{2}\right) \\ \frac{i\Omega^*}{\Omega_R} e^{-i\left(\frac{\Delta t}{2}+\delta_0\right)} sin\left(\frac{\Omega_R t}{2}\right) & e^{-\frac{i\Delta t}{2}}\left[cos\left(\frac{\Omega_R t}{2}\right) + \frac{i\Delta}{\Omega_R} sin\left(\frac{\Omega_R t}{2}\right)\right] \end{bmatrix} \tag{15}$$

This microwave operation matrix rotates the Bloch vector on the Bloch sphere shown in Fig. 5 below.

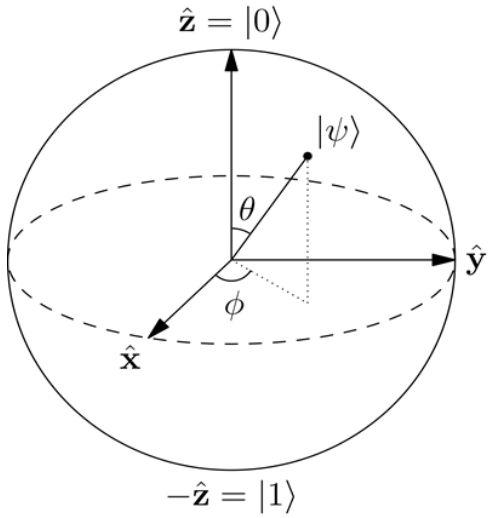

Fig. 5 Rotations on the Bloch sphere.

Rotations about the y −axis of the Bloch sphere correspond to $\delta_0 = \frac{3\pi}{2}$, and these rotations are typically denoted by $R_y(\theta)$, where $\theta = \Omega_R t$ is the rotation angle. Rotations about the x −axis then correspond to $\delta_0 = \pi$ and these rotations are typically denoted by $R_x(\theta)$.

Near resonance we have $\Delta \ll \Omega$, hence $\frac{\Delta}{\Omega_R} \approx 0$ and $\frac{\Omega}{\Omega_R} \approx 1$. In addition, this means that during the typical time of a microwave operation (order π/Ω) that the phase factor $e^{\frac{i\Delta t}{2}} \approx 1$. For Ytterbium 171 ions in our lab, the microwave rotations are implemented experimentally by generating 12.642812118466 GHz pulses with Rhode & Schwarz signal generator and sending the amplified signal into the trap through a vacuum chamber window with a microwave horn. The microwave horn can be re-oriented to optimize the coupling. The greater the power into the trap the bigger the Rabi frequency. The selection rules for magnetic dipole transitions can be derived from the following relation, as outlined in [8],

$$A \propto \langle 0|\hat{L} + 2\hat{S}|1\rangle \tag{16}$$

where $\hat{L}$ and $\hat{S}$ are the total orbital angular momentum operator and total spin angular momentum operator respectively. A transition $|0\rangle \leftrightarrow |1\rangle$ is magnetic dipole allowed if the matrix elements of either total orbital angular momentum operator $\hat{L}$ or total spin angular momentum operator $\hat{S}$ are nonzero. The following is a list of these selection rules as summarized in [8],

1) No change in electronic configuration,
2) Parity is unchanged,
3) $\Delta J = 0, \pm 1$,

4) $\Delta M_J = 0, \pm 1$,
5) $\Delta J = 0$ together with $\Delta M_J = 0$ is not allowed (in particular $J = 0 \leftrightarrow 0$ is not allowed),
6) $\Delta L = 0$,
7) $\Delta L = 0$,

where L, S, J and M_J are the orbital angular momentum, spin angular momentum, total angular momentum, and its projection respectively.

III. PHOTOIONIZATION AND TRAPPING

Electron impact ionization was a widely used method of ionization in the early days of ion trapping and laser cooling, however, photoionization later took over as a preferred method of ionizing neutral atoms due to some advantages it offers, including its relatively high efficiency, no excess charge introduced in the trap as well as its ability to be isotope selective [9], [10], [11], [12]. In [13] Yb atoms are singly ionized using the photoionization laser (398.9 nm) locked to the fluorescence signal of a collimated atomic beam. The first 398.9 nm photon excites a transition $6s^2\ {}^1S_0 \leftrightarrow 6s^2 6p^1\ {}^1P_1$ and the second 398.9 nm photon takes the electron close to the continuum where the field ionization by trap rf field ($> 1000\ V/cm$) pushes the electron into the continuum. Alternatively, after the first 398.9 nm photon excites a transition $6s^2\ {}^1S_0 \leftrightarrow 6s^2 6p^1\ {}^1P_1$, a second photon ($\leqslant 394.5\ nm$) sends the electron into the continuum [13], [9]. These two photoionization approaches are shown in Fig. 6 below.

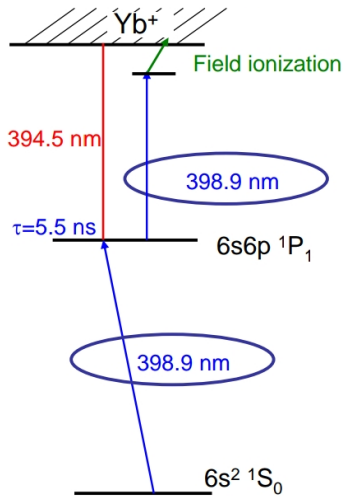

Fig. 6 Two ways to photoionize Ytterbium atoms [13].

In [14], [15] a continuous-wave (CW) titanium-sapphire laser is used to generate, in second harmonic, 399 nm laser beam which excites the $6s^2\ {}^1S_0 \leftrightarrow 6s^2 6p^1\ {}^1P_1$ transition in neutral ytterbium atoms. Another laser kicks the electron into the continuum which results in the ionization of the Ytterbium atom. The loading rate of ytterbium into the trap through photoionization is measured using the electric resonance detection of the secular motion of the trapped ytterbium ions. The electric resonance detection could be carried by driving the trapped ions on resonance with electric pulses applied on the trap electrodes and measuring their response by camera or PMT or by electrical image-current detection. The number of ions in the trap is estimated based on the measured loading rate. In [9] isotope selective two-photon ionization (369 nm and 399 nm), of neutral ytterbium atoms, that allows for efficient loading of ion traps with ytterbium ions. The ionization efficiency is compared with that of electron impact ionization. It is also demonstrated that nearly deterministic loading of a desired number of ions into a linear Paul trap is achievable.

Our strategy for trapping ions is to first produce neutral atoms inside the trapping volume and then photoionize them to achieve trapping. A beam of neutral Ytterbium atoms is produced thermally and sprayed into the linear Paul trap by resistively heating one of our two neutral atom ovens. Each of our ovens is made of stainless steel hypodermic tubing that is bent in a U-shape with an opening in one corner to form a nozzle as shown in Fig. 7 below. Thin strips are cut from Ytterbium sheet and stuffed carefully into the needle resulting in a loaded oven. The ovens are mounted on the side of the trap with nozzles facing towards the trap center and connected via an electrical feed-through to a current source outside the vacuum chamber. As the current passes through the oven, it heats the oven resistively, thus, releasing a spray of neutral Ytterbium atoms into the trap.

This publication is licensed under Creative Commons Attribution CC BY.

Fig. 7 Ytterbium ovens.

These atoms are then ionized through photo-ionization which is a two-photon process. Upon reaching the trap center, first, the atoms are hit with a continuous-wave (CW) Moglab diode laser beam tuned at 398.91 nm, to be on resonance with the ${}^1S_0 \leftrightarrow {}^1P_1$ the transition of neutral Yb. The linewidth of this isotope selection laser is reported in its manual as $< 100\ kHz$. The second laser beam is tuned to 369.53 nm, from a frequency-doubled CW laser source and drives the atom's electron into the continuum where background gas can easily kick it off thus, leaving behind an ionized Yb atom. That is, the 398.91 nm laser beam excites Yb atoms from the ${}^1S_0$ to the ${}^1P_1$ level, from which the 369.53 nm laser beam can promote the electron to the continuum as shown in Fig. 8[5].

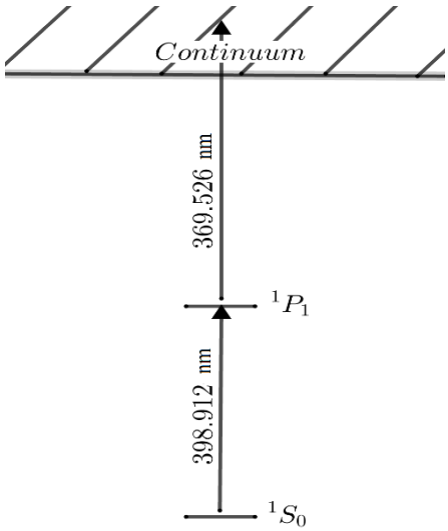

Fig. 7 Ytterbium photoionization.

The atomic source ovens are aligned such that the propagation direction of the neutral Yb atoms is approximately perpendicular to the 398.91 nm beams to minimize Doppler shifts thus, favorable for isotopically selective loading. The 369.53 nm laser beam comes in at three different angles one of which is roughly perpendicular to the 398.91 nm beams while the other one is co-propagating with it. The 398.91 nm diode laser outputs about $4mW$ of which $0.2mW$ gets to one entrance window of the vacuum chamber. A second beam near 369.53 nm is generated by frequency-doubling the light produced by a CW amplified diode laser near 739.05 nm. Approximately 375 mW of 739.05 nm light is sent to a resonant cavity containing a critically phase-matched LBO crystal, producing more than 14 mW at 369.53 nm. One Yb oven is switched on at the time by applying approximately 2 Amp from the current source. Scanning the isotope selection laser we were able to clearly distinguish different isotopes on the following wavelengths; 398.91080 nm, 398.91100 nm, 398.91114 nm, 398.91156 nm, and 398.91170 nm. Moving from one wavelength to the next there was nothing loaded into the trap by photoionization and this explains how sensitive the photoionization was to this laser beam wavelength. The photoionization was insensitive to the scanning of the 369.53 nm laser wavelength as expected.

A. Trapping Parameters

Our RF supply for trapping consists of the function generator, generating a sine wave which is amplitude modulated externally to control the trap depth. We use external amplitude modulation to tune the amplitude since tuning the amplitude directly on the function generator makes some voltage clicks which result in the loss of trapped ions. The voltage clicks could be caused by the function generator probably turning off the output to switch to a different gain regime as one tune the output amplitude. The function generator feeds an rf power amplifier which in turn feeds a helical resonator that connects straight to the trap electrodes. A directional coupler is connected between the amplifier and the resonator to

monitor the back-reflected voltage which calls for tuning of resonator coupling if too much back-reflection is observed. The resonance frequency of our helical resonator sits at about 28 MHz when unloaded and 16.04 MHz when loaded with the trap. The resonator has two probes coupling-out its output for monitoring purposes. One probe is a built-in inductive probe while the other one is a detachable capacitive probe which is usually used for calibration purposes as explained in [19].

In one of our many successful trapping cases, after empirically searching through tuning of various parameters, we had our function generator set up for 16.04 MHz continuous sine wave with 4 V_{pp} and the inductive probe measured 5.04 V. This made the voltage at the trap electrodes be around 227 V since the step-up ratio from the inductive probe to the resonator output measured 45. The back-reflection level was around 600 mV. After some rough trap compensation, the endcap electrode voltages were 50 V and 58 V while the compensation electrode voltages were both 200 V. The oven current was set at 2.1 Amp and the starting vacuum chamber pressure was $1.2E-10$ $Torr$. We observed that it helps to lower rf drive voltage amplitude down and bring it up slowly in cases where trapping seems to be tricky. The ions resided in a two-coil magnetic field of about 3.4 $Gauss$, powered from a current source at 1 Amp, for defining the quantization axis.

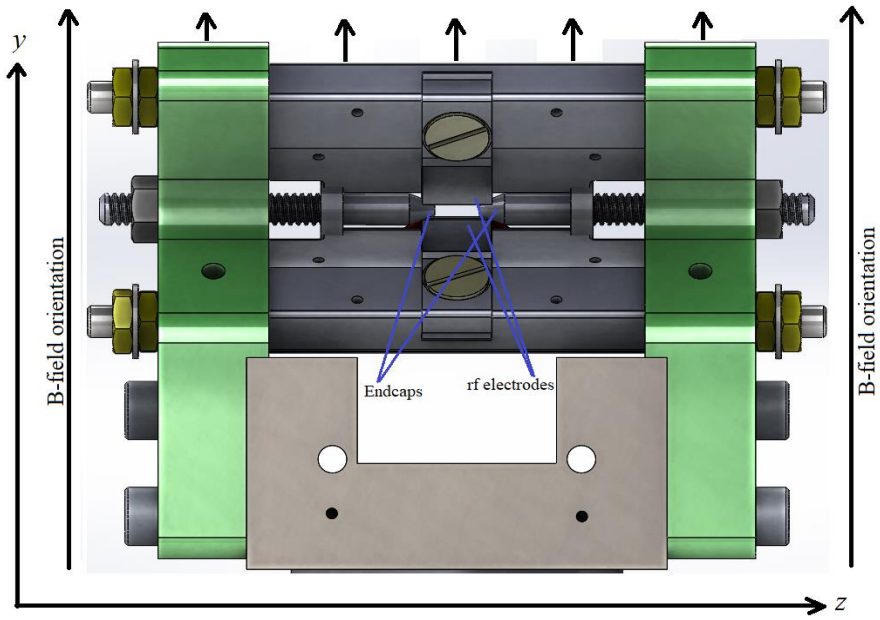

Fig. 9 The direction of the magnetic field relative to the trap [20].

Fig. 9 above shows the magnetic field due to the two coils (one above and another below the trap respectively) is along the vertical or $y-$axis in relation to our trap.

B. Laser Beam Geometry

The laser beams enter the chamber through three different windows as shown in Fig. 10 below. The laser beam combination (Beam 1) going through the big window is horizontal and makes an azimuthal angle of about 20^0 with the trap axis. The laser beams at this window include the 369 nm, 638 nm, and 935 nm laser beams. The laser beam combination (Beam 2) going through the medium window is horizontal and makes an azimuthal angle of about 70^0 with the trap axis. The laser beams at this window include the 369 nm, 398 nm, 638 nm, and 935 nm laser beams.

This publication is licensed under Creative Commons Attribution CC BY.

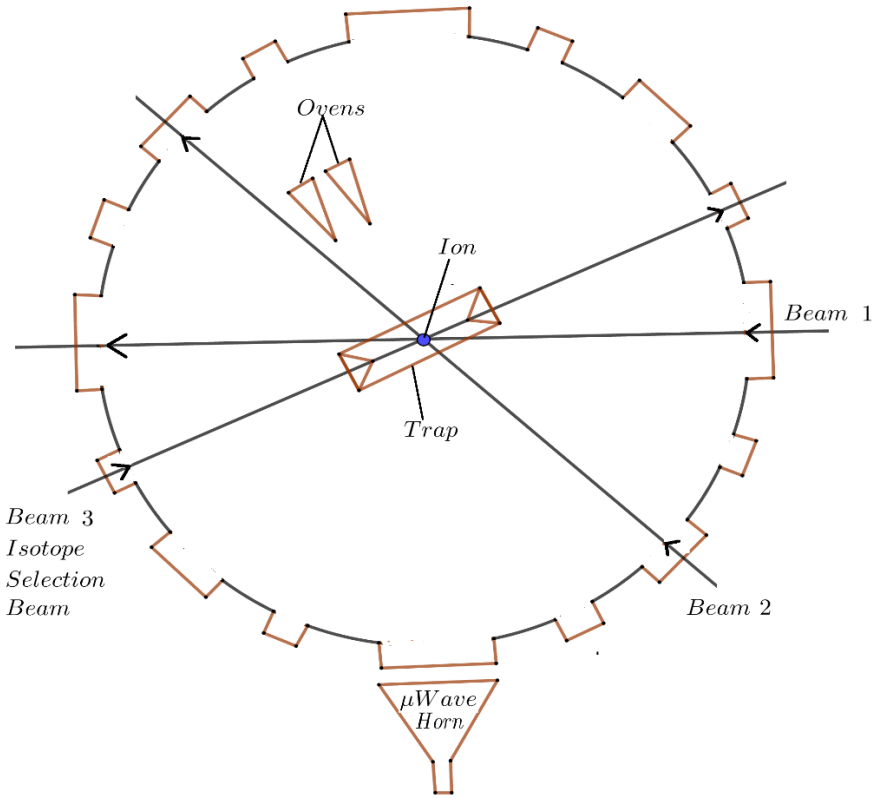

Fig. 10 Laser beams into the chamber.

This angle is preferable for Doppler cooling ions since it is almost perpendicular to ions' motion along the trap axis. The laser beam combination (Beam 3) going through the small top window makes an angle of about 45^0 to the horizontal and is azimuthally aligned with the trap axis as it goes through the trap center from above and exits underneath the trap. The laser beams at this window include the 369 nm, 398 nm, 638 nm, and 935 nm laser beams. This direction of these laser beams makes a right angle with the direction of the neutral atom beam thus, making this an ideal angle for isotope selective photoionization.

C. Doppler Cooling of Ytterbium Ion

A confined Yb^+ ion is Doppler-cooled with the 369 nm laser beam by slightly red-detuning it relative to the ${}^2S_{1/2} \leftrightarrow {}^2P_{1/2}$ a transition is shown in Fig. 11 below.

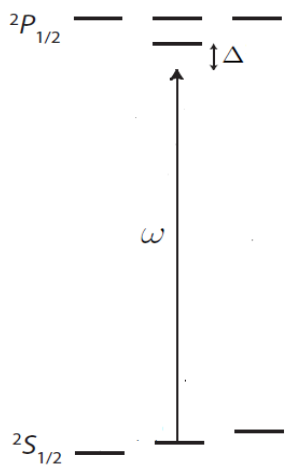

Fig. 11 The red-detuned 369 nm laser on the ${}^2S_{1/2} \leftrightarrow {}^2P_{1/2}$ transition.

The photon scattering rate of the atom is affected by the laser frequency detuning and this is the key principle in Doppler cooling as shown below, [5],

$$\Gamma_{sc} = \frac{\frac{I}{I_{sat}} \frac{\Gamma}{2}}{1+\frac{I}{I_{sat}}+\frac{4\Delta_I^2}{\Gamma^2}} \tag{17}$$

with Γ_{sc}, Γ, I, I_{sat} and Δ_l as ion's scattering rate, the spontaneous emission rate of the transition, incident laser beam intensity, saturation intensity, and incident laser beam detuning respectively. Detuning the incident light to the red of the transition's resonance, an atom moving towards the light will scatter more photons than it does while moving in the opposite direction and this allows a trapped ion to be cooled. It is favorable to set up the incident cooling laser beam such that it has non-vanishing spatial components in all of the principal axes of the trap so that a single beam of incident light can cool the motion of trapped ions in all directions. With Doppler cooling, it can be shown that the minimum temperature T_{Dmin} achievable is at a detuning $\Delta_l = -\Gamma/2$, and is given by,

$$T_{Dmin} = \frac{\hbar\Gamma}{2k_B} \tag{18}$$

The $^2S_{1/2} \leftrightarrow {}^2P_{1/2}$ Yb transition yields a theoretical Doppler cooling limit of 470 μK. In the experiment, we typically Doppler cool the Ytterbium atom on the $^2S_{1/2} \leftrightarrow {}^2P_{1/2}$ transition with 369.53 nm laser beam. Using only 369 nm laser beam to cool trapped ions is not efficient precisely because the $^2P_{1/2}$ the state does not only decay to the $^2S_{1/2}$ level but also decays to the metastable $^2D_{3/2}$level about 0.5% of the time. To remedy this problem an optical pumping laser beam at 935.2 nm is used to drive the ion from the $^2D_{3/2}$ to the $^3[3/2]_{1/2}$ level, from which it quickly decays back to $^2S_{1/2}$ level in the cooling transition. The trapped ion can also fall into the $^2F_{7/2}$ state and another optical pumping laser beam near 638.6 nm is used to depopulate the $^2F_{7/2}$ level, returning the ion to the cooling cycle [16]. Fig. 12 below (from [5]) shows transitions involved during the Doppler cooling process of Ytterbium 171 ion.

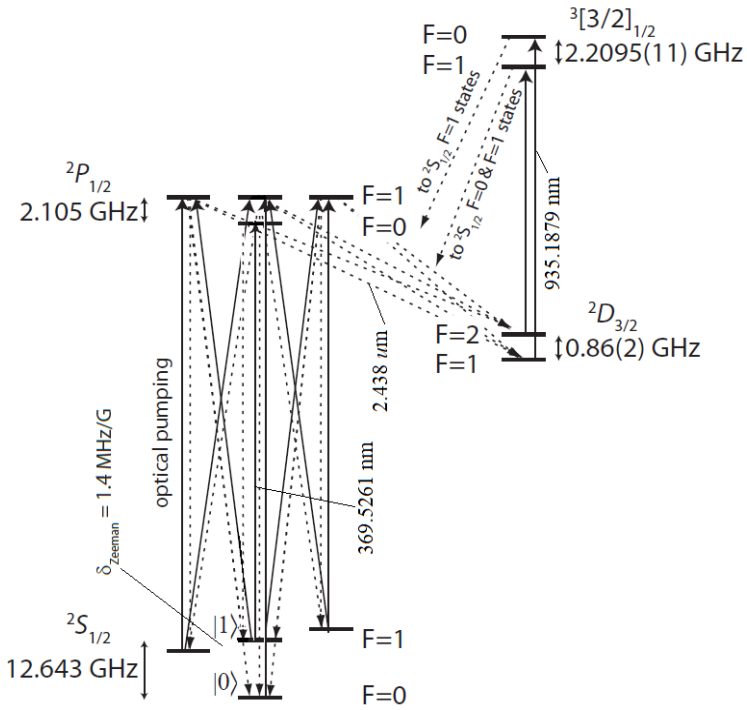

Fig. 12 Summary of the cooling cycle [5].

In the case of the Ytterbium 171 ion, there is an addition of the hyperfine structure. In this case off-resonance scattering in the Doppler cooling transition $^2S_{1/2}|F=1\rangle \leftrightarrow {}^2P_{1/2}|F=0\rangle$ ends up populating the dark state $^2S_{1/2}|F=0\rangle$. To prevent this during cooling intervals, the 369:53 nm is passed through a 14.7 GHz resonant traveling wave Qubig (EOWG14.7M2) EOM to generate sidebands 14.7 GHz away from the carrier 369.53 nm. The blue sideband drives the transition $^2S_{1/2}|F=0\rangle \leftrightarrow {}^2P_{1/2}|F=1\rangle$ which brings the ion back to the cooling cycle. Population trapping in the $^2D_{3/2}|F=1\rangle$ manifold is avoided by the presence of a laser at 935.2 nm, which rapidly returns the atom to the cooling cycle via the transition $^2D_{3/2}|F=1\rangle \leftrightarrow {}^3[3/2]_{1/2}|F=0\rangle$. The $^3[3/2]_{1/2}|F=0\rangle$ decays preferentially to $^2S_{1/2}$. About 600 μW of 935.2 nm light is sent into the trap, focused to a spot with a waist of approximately 200 μm. When the ion is excited off-resonantly to the $^2P_{1/2}|F=1\rangle$ manifold during cooling, the ion may decay to $^2D_{3/2}|F=2\rangle$. We depopulate this level by using a fiber EOM driven at 3.0695 GHz which adds sidebands on 935.2 nm light, one of which is resonant with the $^2D_{3/2}|F=2\rangle \leftrightarrow {}^3[3/2]_{1/2}|F=1\rangle$ transition. Fig. 13 shows a schematic of 935 nm laser beam passing through the fiber EOM on its way to the trap.

This publication is licensed under Creative Commons Attribution CC BY.

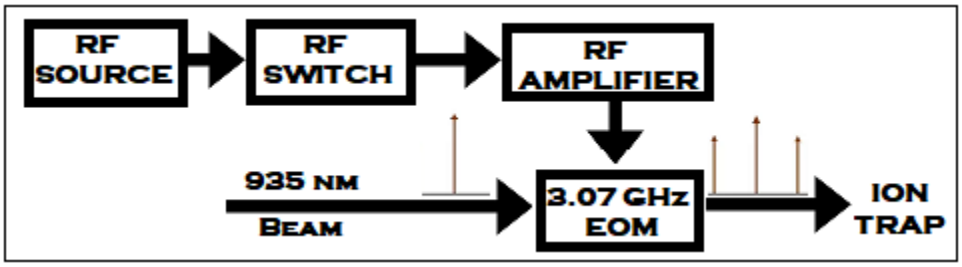

Fig. 13 Schematic of 935 nm laser beam through the 3.07 GHz EOM.

A Fabry-Perot and oscilloscope were used to observe the generated sidebands on the 935 nm beam. Fig. 14 below shows the sidebands generated on 935 nm laser beam.

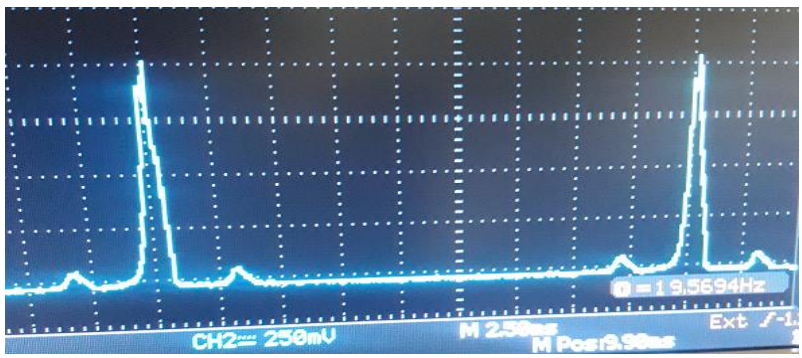

Fig. 14 The 3.07 GHz EOM sidebands.

Finally the $^2F_{7/2}$ hyperfine levels are depopulated by laser light switched between 638.6102 nm and 638.6151 nm to drive the transitions $^2F_{7/2}|F=3\rangle \leftrightarrow {}^1[5/2]_{5/2}|F=2\rangle$ and $^2F_{7/2}|F=4\rangle \leftrightarrow {}^1[5/2]_{5/2}|F=3\rangle$ respectively. Nearly 1 mW of 638.6 nm light is present at the trap, focused to about 200 μm.

IV. RABI-FLOPS WITH YTTERBIUM 171 QUBITS

The odd isotopes of Ytterbium have a hyperfine structure that can be used for qubit realization [17]. For instance, Ytterbium 171 ion has a level structure shown in Fig. 15 which shows the hyperfine structure in the $^2S_{1/2}$ manifold.

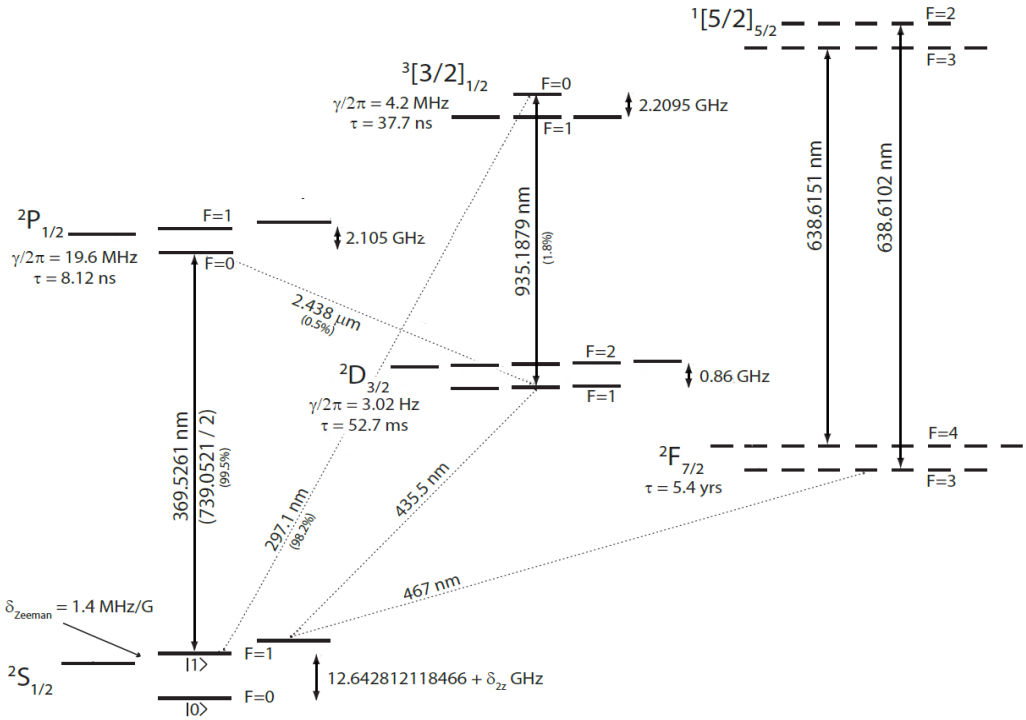

Fig. 15 Level structure for Ytterbium 171 ion.

The transition $^2S_{1/2} \leftrightarrow {}^2P_{1/2}$ is good for both state detection and Doppler cooling. In this section, we manipulate the trapped Ytterbium 171 ion qubit with microwave pulses and demonstrate Rabi oscillations with a cloud of trapped ions. We note that, to our knowledge, this is the first demonstration of coherent manipulation of memory qubits in South Africa. To date, the only other realization of qubits was in the form of entangled photons [18]. We abbreviate the hyperfine states $^2S_{1/2}|F = 0\rangle$ and $^2S_{1/2}|F = 1, m_F = 0\rangle$ as qubit states $|0\rangle$ and $|1\rangle$ respectively. The presence of other transitions in Fig. 15 is indicative of the need for re-pumping and cooling cycle lasers. EOMs are required to switch on and off some sidebands during the experiments which involve four phases of cooling, state preparation, state evolution, and state detection. These three phases are outlined next in an experiment aimed at demonstrating Rabi oscillations. A 369.53 nm laser beam is split into two beams each of which is double-passed through one of two AOMs resulting in two beams shifted by 220 MHz on the second pass. In our implementation, the purpose of the AOMs is not necessary to shift the laser frequency but rather to provide a switching control mechanism for the laser beam. That is, each of the two laser beams can be switched on and off independently using an FPGA program that controls the RF supply going to the AOMs.

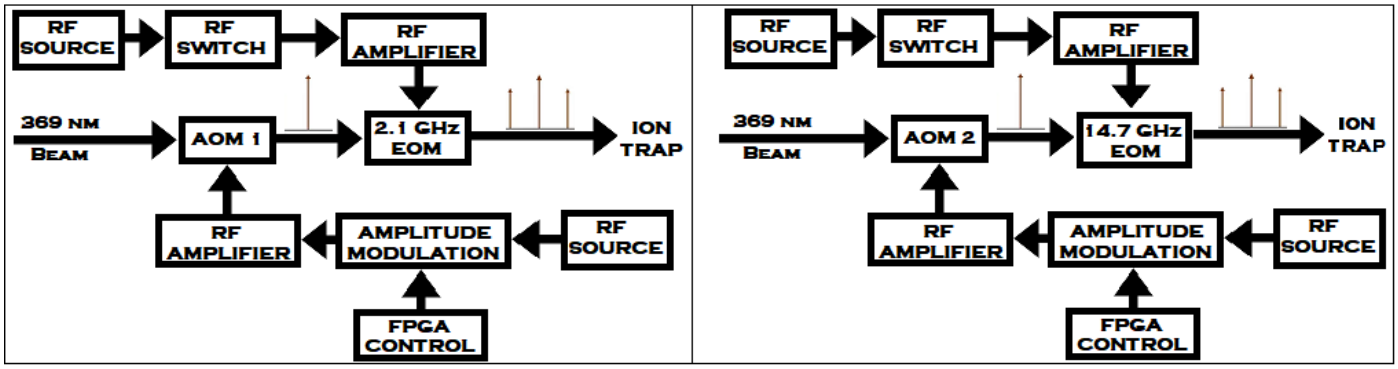

Fig. 16 Schematics of the 369 nm beam pathway through 2.1 GHz EOM (Left) and 14.7 GHz EOM (Right) to the trap.

One beam from the AOMs is passed through the 2.1 GHz Qubig (E0-T2100-M3) EOM, while the other beam is passed through a 14: 7 GHz Qubig (EO-WG14.7M2) EOM to generate necessary sidebands before reaching the trapped ions. Fig. 16 shows the schematic of the 369 nm beam pathway through AOMs and EOMs on their way to the trap. Each of the EOMs has an rf supply and an FPGA-controlled rf switch. The rf switches allow the sidebands to be turned on and off independently through the FPGA program. Fig. 17 below shows the sidebands for both EOMs measured with a Fabry-Perot and oscilloscope.

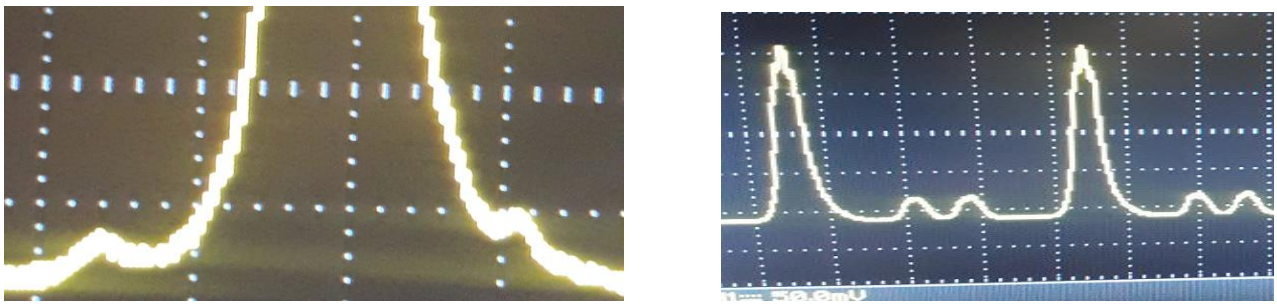

Fig. 17 Left: 2.1 GHz sidebands on 369 nm laser beam. Right: 14.7 GHz sidebands on 369 nm laser beam.

A. State Preparation

The aim of optical pumping in this stage of the experiment is to prepare the state of the Ytterbium 171 ion qubit into the dark state $|0\rangle$. To prepare in the dark state the 14.7 GHz sidebands are turned off so that ions in the dark state do not get rescued out. Also, the 2.1 GHz EOM is turned on for an efficient coupling/scattering to the level $^2P_{1/2}|F = 1\rangle$ which then decays to the dark state. That is the EOM generates a blue sideband resonant with the transition $^2S_{1/2}|F = 1\rangle \leftrightarrow {}^2P_{1/2}|F = 1\rangle$. The 3.07 GHz EOM is also turned on to depopulate the metastable $^2D_{3/2}$ level as a means to facilitate efficient state preparation with high fidelity and so it does not get stuck there. Fig. 18 below gives a summary of involved transitions during state preparation [5].

This publication is licensed under Creative Commons Attribution CC BY.

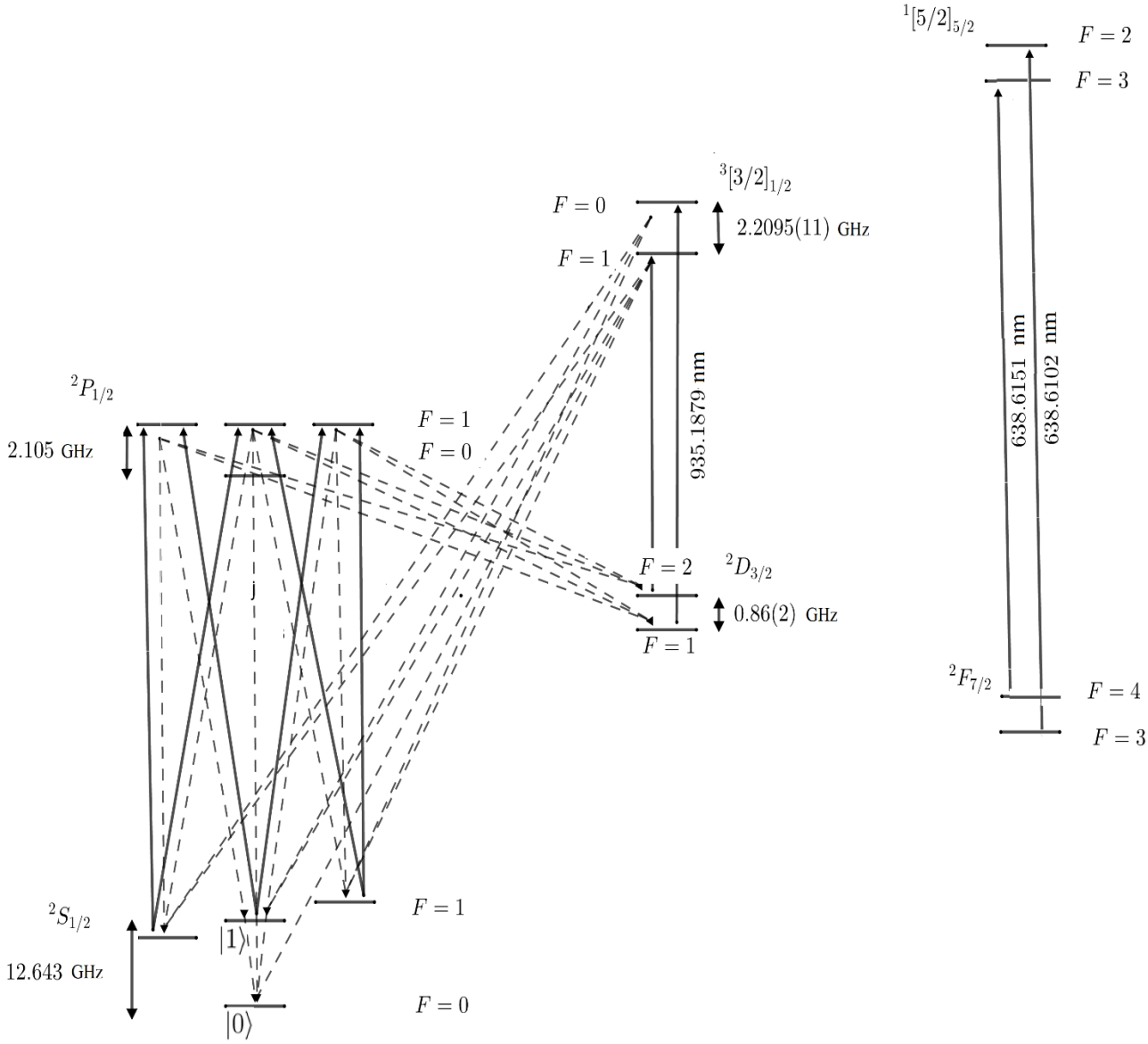

Fig. 18 State preparation into the dark state.

In our Rabi oscillations experiment, we state-prepared for 100 μs after cooling for 100 ms.

B. State Evolution

As explained in Section II, we can rotate the state of the ion between $|0\rangle$ and $|1\rangle$ by applying microwaves resonant with the 12.643 GHz transition in $^2S_{1/2}$ manifold. Fig. 19 below shows the evolution of the qubit state back and forth between these two states.

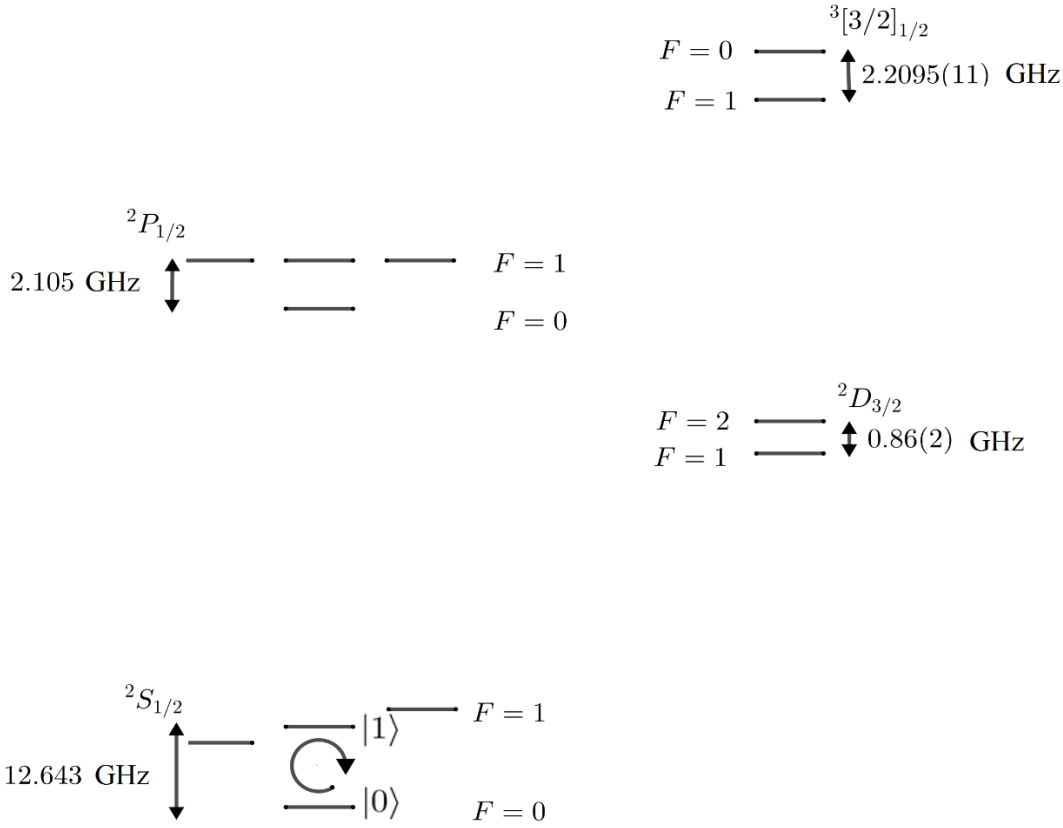

Fig. 19 State evolution with microwave pulses.

We apply these microwave pulses for varying times to trace out the evolution of the qubit state. In our experiment, we start with a microwave duration of zero seconds and keep incrementing by 1 μs. For each time increment, we made 50 measurements and averaged them before introducing another time increment. And for each measurement we cool, state-prepare, state-evolve, and state-detect. During state evolution both the 14.7 GHz EOM and 369 nm laser beam are is switched off to avoid creating a pathway for ions out of the $|0\rangle \leftrightarrow |1\rangle$ state evolution transition. The 2.1 GHz EOM was also off but that does not matter much. The 369 nm laser beam was turned on and off using the AOMs instructed by the FPGA program.

C. State Detection

A critical step in quantum computation and communication protocols is the detection of the qubit state. In ytterbium 171 ion, state detection is accomplished using standard ion fluorescence techniques. The 369.53 nm light of the detect beam is tuned to be nearly in resonance with the $^2S_{1/2}|F = 1\rangle \leftrightarrow {}^2P_{1/2}|F = 0\rangle$ transition. Fig. 20 below shows the involved transitions during state detection [5]. If the ion is prepared in the $|0\rangle$ state, this incident light is detuned from $^2P_{1/2}|F = 1\rangle$ by 14.7 GHz, and thus, the ion scatters very few photons. The state of the ion is determined by the number of photons observed by the PMT during the detection interval.

This publication is licensed under Creative Commons Attribution CC BY.

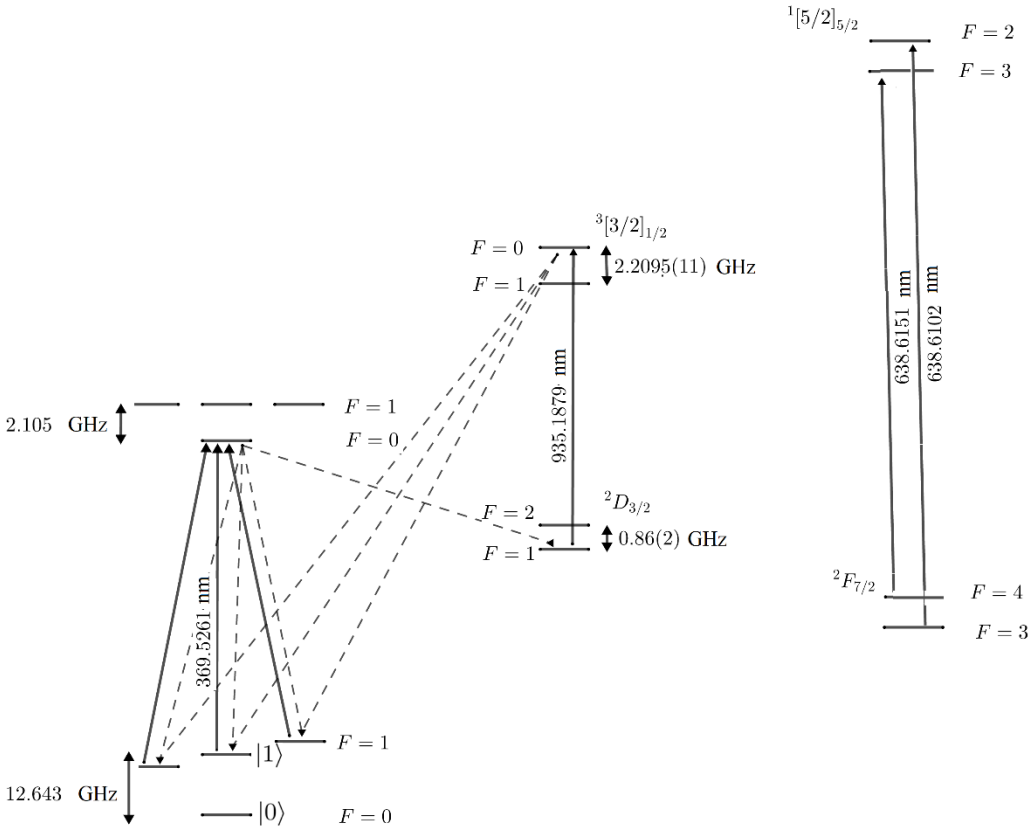

Fig. 20 State detection with 369 nm laser beam.

Since the initial state is $|0\rangle$, the incident light is detuned from the $^2P_{1/2}|F = 1\rangle$ manifold by 14.7 GHz and the transitions to the level $^2P_{1/2}|F = 0\rangle$ are forbidden by selection rules. Taking into account decay to the $^2D_{3/2}$ level reduces the total number of 369.53 nm photons scattered by the ion. In addition, off-resonant coupling to the level $^3[3/2]_{1/2}|F = 1\rangle$ may occur while depopulating the $^2D_{3/2}\,|F = 1\rangle$ manifold.

D. Rabi flops

Fig. 21 below shows the Rabi oscillation produced by the experiment described above with time steps (for microwave pulse duration) of 1 μs, cooling time of 100 ms, state preparation time of 100 μs and state detection time of 10 ms. The working laser wavelengths were parked (free-running) at 398.91095 nm, 638.614 nm, 739.0524 nm, and 935.1878 nm while the pressure was $1.50E-9\,Torr$. This is about two orders of magnitude higher pressure than an intended target of $\sim 1E-11\,Torr$. At this $1.50E-9\,Torr$ pressure, when trapping a few ions in a cooled crystal, one observes frequent crystal rearrangements which we interpret as the result of collisions with background gas molecules and the repetitive heating and cooling of ions by free-running (i.e. unlocked) 739.0524 nm laser. The Rabi oscillations curve below has a decaying amplitude which we attribute not to the loss of coherence, but rather to the loss of ions from the trap as a consequence of chemistry with the background gas molecules. We conclude this firstly because we expect the coherence time of the ion to be significantly longer since we are driving a clock transition and our microwave source is locked to Stanford Research Systems FS725 Rubidium Atomic clock. And secondly, because the loss of coherence should lead to a loss of oscillation contrast that tends to the halfway point between maximum and minimum fluorescence, rather than damping out completely. We lost the whole cloud at around 286 μs, however, the Rabi oscillations are evident with a period of 34.7 μs approximately.

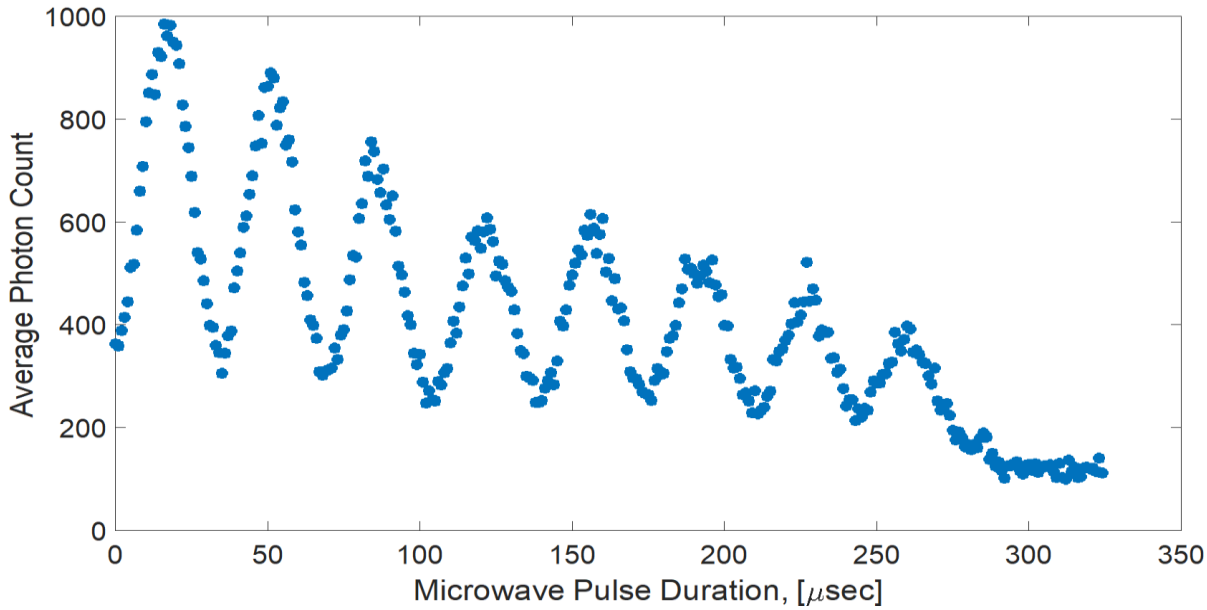

Fig. 21 Trapped Ytterbium 171 ions Rabi flops.

In this experiment, the initial total fluorescence count in 10 ms of fluorescence collection was ~1160 photon counts, with a background count of ~130 photons. The Rabi oscillation in Fig. 21 does not attain full contrast oscillations between these two limits. This indicates that we likely have imperfect initial state preparation and that the quantum state of the ions is best described by a mixed state density matrix at the beginning of the experiment. In other words, some (classical) fraction of the ions remains in the upper state at the end of the optical pumping step. To properly interpret the dynamics Mathematically, we have to adapt the wavefunction description given in Section II to the density matrix picture. To that end, we define the following variables

$$\tilde{c}_0 = c_0 e^{-\frac{i\Delta t}{2}} \tag{19}$$

$$\tilde{c}_1 = c_1 e^{+\frac{i\Delta t}{2}} \tag{20}$$

and substitute them in equations $(6-7)$ to obtain,

$$\dot{\tilde{c}}_0 = -\frac{i}{2}\left(\Omega \tilde{c}_1 e^{+i\delta_0} + \Delta \tilde{c}_0\right) \tag{21}$$

$$\dot{\tilde{c}}_1 = -\frac{i}{2}\left(\Omega \tilde{c}_0 e^{-i\delta_0} - \Delta \tilde{c}_1\right) \tag{22}$$

We now define a density matrix $\rho(t)$ as follows,

$$\rho(t) = \begin{bmatrix}\tilde{c}_0\\ \tilde{c}_1\end{bmatrix}\begin{bmatrix}\tilde{c}_0^* & \tilde{c}_1^*\end{bmatrix} = \begin{bmatrix}|\tilde{c}_0|^2 & \tilde{c}_0\tilde{c}_1^*\\ \tilde{c}_1\tilde{c}_0^* & |\tilde{c}_1|^2\end{bmatrix} = \begin{bmatrix}\rho_{00} & \rho_{01}\\ \rho_{10} & \rho_{11}\end{bmatrix} \tag{23}$$

with ρ_{00} and ρ_{11} as percentage populations for ground and excited states respectively, ρ_{01} and ρ_{10} are associated with coherence. Using equations $(19-22)$ we obtain the following set of first-order differential equations in density matrix elements,

$$\dot{\rho}_{11} = -\dot{\rho}_{00} = 2\tilde{c}_1\dot{\tilde{c}}_1^* = \frac{i\Omega}{2}(\rho_{10}e^{+i\delta_0} - \rho_{01}e^{-i\delta_0}) \tag{24}$$

$$\dot{\rho}_{01} = \dot{\rho}_{10}^* = \tilde{c}_0\dot{\tilde{c}}_1^* + \dot{\tilde{c}}_0\tilde{c}_1^* = \frac{i\Omega}{2}(\rho_{00} - \rho_{11})e^{+i\delta_0} - \Delta\rho_{10} \tag{25}$$

From equations $(24-25)$ we can arrive at the following set of equations (by setting $e^{\pm i\delta_0} = 1$ and $\Delta = 0$ i.e on-resonance excitation) which is similar in form to equation set (7.42) in [6].

$$\dot{\rho}_{11} = -\dot{\rho}_{00} = \frac{i\Omega}{2}(\rho_{10} - \rho_{01}) \tag{26}$$

$$\dot{\rho}_{01} = \dot{\rho}_{10}^* = \frac{i\Omega}{2}(\rho_{00} - \rho_{11}) \tag{27}$$

with Ω as the Rabi frequency. The previous set of equations can be rewritten as the following second-order differential equation in ρ_{11},

$$\ddot{\rho}_{11} + \Omega^2\rho_{11} - \frac{\Omega^2}{2} = 0 \tag{28}$$

This publication is licensed under Creative Commons Attribution CC BY.

Solving this second-order differential equation (with initial conditions $\rho_{11}(t = 0) = a$, $\dot{\rho}_{11}(t = 0) = 0$ we obtain the following solution,

$$\rho_{11} = \frac{1}{2}((2a - 1)\,cos(\Omega t) + 1) \tag{29}$$

To account for the ion loss from our cloud we consider $N(t)$ ions at time t in the cloud and assume the ion loss rate due to collisions is proportional to the number of ions. In other words, $\dot{N} = -N\tau^{-1}$ whose solution is given by,

$$N(t) = N_0 e^{-\frac{t}{\tau}} \tag{30}$$

Multiplying equation (28) by equation (30) we obtain the fraction of ions $N(t)\ \rho_{11}\ (t)$ in the excited state and this quantity is proportional to the average photon count $P_c(t)$,

$$P_c(t) = N(t)\rho_{11}\ (t) = \frac{N_0}{2} e^{-\frac{t}{\tau}}\big((2a - 1)\,cos(\Omega t) + 1\big) + P_{c0} \tag{31}$$

with P_{c0} as the average background photon count. The model in equation (31) above was used to fit the average photon count data, with $P_c(t)$ being the average photon count as a function of microwave pulse duration, t. Fig. 22 below shows the plot of the data along with the fitting model as described by equation (31).

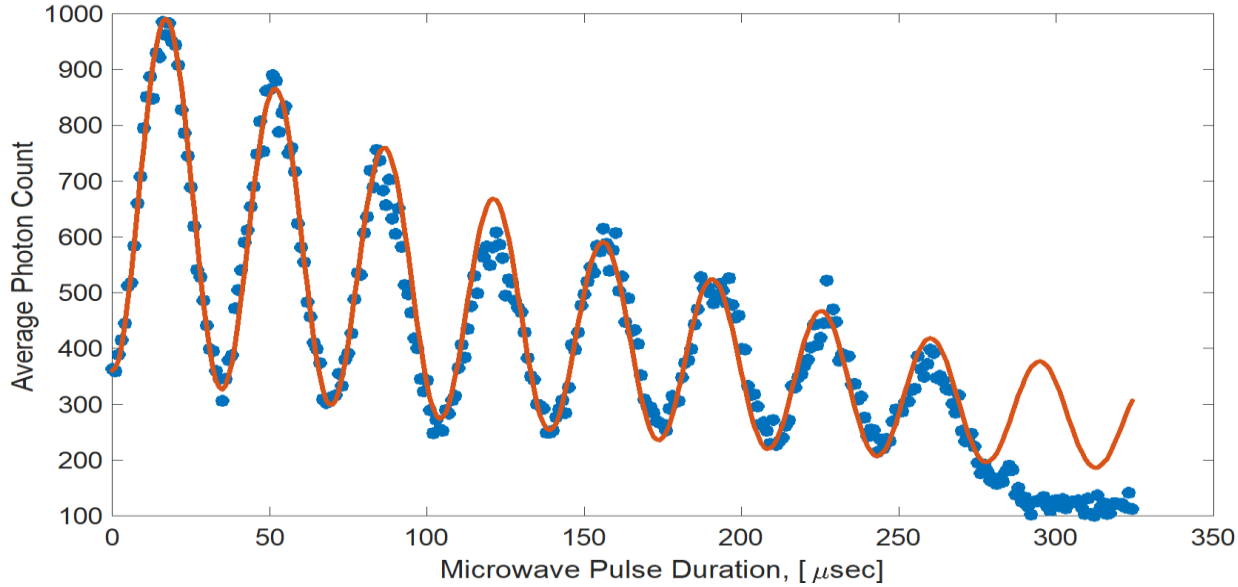

Fig. 22 Trapped Ytterbium 171 ions Rabi flops model with fitted data.

The initial cloud was composed of approximately $N_0 = 1160$ photons (i.e. at $t = 0\,sec$). Time constant $\tau = 4500^{-1}$ seconds is related to the time it takes ions to be lost from the trap, Rabi frequency $\Omega = 181\ kilorad/s$, the percentage of initial ions in the excited state was $a = 230/N_0$ and the average background photon count $P_{c0} = 130$ photons. A different approach to the timing of our measurements would allow us to see longer-lived oscillations even in the presence of the ion loss, albeit with reduced initial amplitude. Instead of taking 50 measurements at one point in time and averaging those measurements before stepping in time to the next point, we propose to take one measurement per point, and only after completing the trajectory do we repeat the measurements tracing out another trajectory until we have 50 trajectories to average. In this way, the misfortune of ion loss is distributed almost evenly across the trajectory instead of only towards the end of the trajectory.

V. CONCLUSION

In this paper, we have presented the dynamics of interactions between laser radiation and a confined atom or ion. Laser beams were set up and aligned in a way to allow for isotope selective photoionization of Ytterbium atoms as a two-photon process involving 398 nm and 369 nm lasers. The cooling laser beam was made present at various angles to allow for Doppler cooling in different modes. The manipulation of trapped Ytterbium 171 ion qubits with microwaves was demonstrated through Rabi flops experiment which involved a repetition of Doppler cooling, state preparation with the help of the 2.1 GHz EOM, state evolution with microwaves, and state detection with 369 nm laser fluorescence scattering captured by the PMT for enhancement. The high ion loss rate (with time constant $\tau = 4500^{-1}$) in the Rabi flops experiment is likely due to several factors including, among others, the freely-running (unlocked) lasers, ion collisions with background gas under the existing high-pressure conditions. Regardless of the unfavorable conditions under which the experiment was run, the results (Rabi flops at Rabi frequency $\Omega = 181\ kilorad/s$) obtained were sufficient to demonstrate that we can trap Ytterbium ions successfully and manipulate trapped Ytterbium 171 ions as well. To our knowledge, this was the first realization and demonstration of coherent manipulation of trapped ion memory qubits in South Africa.

REFERENCES

[1] Ozeri R. Tutorial: The trapped-ion qubit tool box. Contemporary Physics: arXiv:1106.1190v1 [quant-ph], 00:1 – 23, 2011.
[2] National Academies of Sciences Engineering and Medicine. Quantum Computing: Progress and Prospects. The National Academies Press, Washington, DC, 2019.
[3] Lucas D. M., Donald C. J. S., Home J. P., McDonnell M. J., Ramos A., Stacey N., Stacey J. P., Steane A. M., Webster S. C. Oxford ion-trap quantum computing project. Phil. Trans. R. Soc. Lond. A, 361:1401 – 1408, 2003.
[4] Brown N. C., Brown K. R. Comparing Zeeman qubits to hyperfine qubits in the context of the surface code: 174yb+ and 171yb+. arXiv:1803.0254v2 [quant-ph], pages 1 – 7, 2018.
[5] Olmschenk S. M. Quantum Teleportation Between Distant Matter Qubits. Ph.D. thesis, University of Michigan, 2009.
[6] Foot C. J. Atomic Physics. Oxford University Press, 2007.
[7] Moya-Cessa H., Soto-Eguibar F., Vargas-Martinez J. M., Juarez-Amaro R., Zuniga-Segundo A. Ion-laser interactions: The most complete solution. Physics Reports, 513:229 – 261, 2012.
[8] Andrew J. S. Hamilton. Apas 5110. internal processes in gases: Transition probabilities and selection rules. Technical report, Joint Institute for Laboratory Astrophysics, 1999.
[9] Johanning M., Braun A., Eiteneuer D., Paape C., Balzar., Neuhauser W., Wunderlich C. Resonance enhanced isotope selective photoionization of Yb for ion trap loading. arXiv:0712.0969v2 [physics.atom-ph], 2010.
[10] Mortensen A., Lindballe J. J. T., Jensen I. S., Staanum P., Voigt D., Drewsen M. Phys. Rev. A 69(4), page 042502, 2004.
[11] Kjaergaard N., Hornekaer L., Thammesen A., Videsen Z., Drewsen M. Appl. Phys. B 71, page 207, 2000.
[12] Gulde S., Rotter D., Barton P., Schmidt-Kaler F., Blatt R., Hogervorst W. Appl. Phys. B 73, page 861, 2001.
[13] Wang L. B., Nguyen T., Schauer M., Torgerson J., Lamoreaux S., Diddams S., Flambaum V. Efficient photoionization loading of ytterbium and indium ion traps. 2007.
[14] Onoda Y. Trapping of Yb+ Loaded through Photoionization in RF Ion Trap. Ph.D. thesis, Kyoto University, 2011.
[15] Onoda Y., Sugiyama K., Ikeda M., Kitano M. Loading rate of yb+ loaded through photoionization in radiofrequency ion trap. Applied Physics B, 105:729 – 740, 2011.
[16] Jau Y. Y., Hunker J. D., and Schwindt P. D. D. F-state quenching with ch4 for buffer-gas cooled 171yb+ frequency standard. AIP Advances, 5:117209–1 – 117209–8, 2015.
[17] Pandey K., Singh A. K., Kumar P. V. K., Suryanarayana M. V., Natarajan V. Isotope shifts and hyperfine structure in the 555.8 nm 1s0 - 3p1 line of Yb. Physical Review A, 80:022518–1 – 022518–6, 2009.
[18] Ismail Y., Joshi S., Forbes A., Petruccione F. Instrumentation limitation on a polarization-based entangled photon source. Journal of the Optical Society of America B, 34:1084 – 1089, 2017.
[19] Matjelo N. J., Khanyile N., Uys H. Design, Implementation and Characterization of Helical Resonator for Ion Trapping Applications. International Journal of Modernization in Engineering Technology and Science, 3(5):1285-1295.
[20] Matjelo N. J., Khanyile N., Uys H. Design, Assembly and Geometric Characterization of Linear Paul Trap using Solidworks, Microscope, and Collimated Laser Beam. International Journal of Science and Research, 10(5):528-535.

This publication is licensed under Creative Commons Attribution CC BY.